Smart Structures and Systems, *Vol. 25, No. 3 (2020) 369-384*
DOI: https://doi.org/10.12989/sss.2020.25.3.369

Sparse reconstruction of guided wavefield from limited measurements using compressed sensing

Baijie Qiao [1,2], Zhu Mao*[2], Hao Sun [3], Songmao Chen [2] and Xuefeng Chen [1]

[1] *The State Key Laboratory for Manufacturing Systems Engineering, Xi'an, 710061, PR China*
[2] *Department of Mechanical Engineering, University of Massachusetts Lowell, Lowell, MA 01854, USA*
[3] *Department of Civil Engineering, Northeastern University, Boston, MA 02115, USA*

(*Received April 18, 2019, Revised May 27, 2019, Accepted July 12, 2019*)

Abstract. A wavefield sparse reconstruction technique based on compressed sensing is developed in this work to dramatically reduce the number of measurements. Firstly, a severely underdetermined representation of guided wavefield at a snapshot is established in the spatial domain. Secondly, an optimal compressed sensing model of guided wavefield sparse reconstruction is established based on l_1-norm penalty, where a suite of discrete cosine functions is selected as the dictionary to promote the sparsity. The regular, random and jittered undersampling schemes are compared and selected as the undersampling matrix of compressed sensing. Thirdly, a gradient projection method is employed to solve the compressed sensing model of wavefield sparse reconstruction from highly incomplete measurements. Finally, experiments with different excitation frequencies are conducted on an aluminum plate to verify the effectiveness of the proposed sparse reconstruction method, where a scanning laser Doppler vibrometer as the true benchmark is used to measure the original wavefield in a given inspection region. Experiments demonstrate that the missing wavefield data can be accurately reconstructed from less than 12% of the original measurements; The reconstruction accuracy of the jittered undersampling scheme is slightly higher than that of the random undersampling scheme in high probability, but the regular undersampling scheme fails to reconstruct the wavefield image; A quantified mapping relationship between the sparsity ratio and the recovery error over a special interval is established with respect to statistical modeling and analysis.

Keywords: guided wavefield; compressed sensing; sparse measurements; laser Doppler vibrometer; full-field reconstruction; piezoelectric structural health monitoring

1. Introduction

Ultrasonic guided waves are widely used in the communities of structural health monitoring (SHM) and nondestructive evaluation (NDE) of plate-like structures due to their low attenuation and high sensitivity to damages (Su *et al*. 2006, Xiang *et al*. 2014, Hong *et al*. 2017, Song *et al*. 2017). Currently, piezoelectric transducers (PZTs) as conventional contact-type sensors are widely used to generate and measure ultrasonic guided waves on structures, and then hidden damages can be identified by comparing the measured signals with the baseline signals from the pristine status (Lu *et al*. 2010). However, the comparison depends on a wealth of physical information such as dispersive relation, and usually leads to increased false alarm rates under harsh environments such as varying temperature and radioactive conditions. Additionally, in order to identify and localize small defects, a dense array of PZTs are demanded, but such installation is costly and labor-intensive.

Recently, the scanning laser Doppler vibrometer (SLDV) system as a noncontact technique for measuring the out-of-plane velocity in a grid of equispaced points over the structure surface is gaining prominence due to its noninvasive nature and highly spatial resolution (Flynn and Jarmer 2013, Chen *et al*. 2018a, b, Staszewski *et al*. 2004, Park *et al*. 2010). In this case, the ultrasonic wavefield image at the user-defined space over the structure surface can be acquired by SLDV. Comparing with the spatially limited contact-type sensors, SLDV can acquire the information of full wavefield data, also known as full wavefield measurements. In particular, the visualization of wave propagation can show the interaction of guided wave with structural damage, which enables automated and intuitive damage diagnosis without any baseline data. Numerous structural health monitoring approaches based on guided waves rely on the understanding of wavefields recorded by SLDV (Staszewski *et al*. 2004, Park *et al*. 2010, 2014, Xiang *et al*. 2012, Di Ianni *et al*. 2015, Sohn *et al*. 2011). For instance, Sohn *et al.* (2011) used a fixed actuator to generate the guided wave and used SLDV to measure the corresponding guided wave for detecting delamination in a composite plate. Park *et al*. (2014) used SLDV to measure the ultrasonic guided wave for identifying and visualizing the hidden delamination in a GFRP wind turbine blade and debonding in CFRP aircraft. In practical applications, since the signal-noise-ratio of a single scan of SLDV is quite low, multiple time traces for

---

∗Corresponding author, Ph.D.,
E-mail: zhu_mao@uml.edu

http://www.techno-press.org/?journal=sss&subpage=7

ISSN: 1738-1584 (Print), 1738-1991 (Online)

averaging are commonly acquired at each scan point to reduce the effect of acquisition noise. Meanwhile, a large number of measurements are required to avoid spatial aliasing of the wavefield image. Therefore, the scanning acquisition process is usually time-consuming, particularly when the structure surface is large and the required measurement grid for wave propagation is dense.

There is a recognized requirement to reduce the acquisition time by reducing the number of acquisitions in the spatial domain. If the wavefield image can be known to be sparse or compressible using a certain transform such as Fourier transform and wavelet transform, a novel sampling approach based on compressed sensing (CS) can be applied to reduce the number of measurements. Compressive sensing theory exploits the fact that most natural signals such as waves, possess a sparse representation in other transforming domain, and demonstrates the effectiveness for recovering signals from limited measurements without loss of information (Candes and Wakin 2008). CS has been used in a wide variety of applications, including the single pixel camera (Duarte *et al*. 2008), SHM (Ginsberg *et al*. 2018, Yang *et al*. 2017 and 2019), source identification (Qiao *et al*. 2016) and seismology (Herrmann *et al*. 2012). For instance, a monotonic iterative shrinkage/thresholding algorithm of compressed sensing was developed for image restoration from 40% missing samples in an underdetermined case (Bioucas-Dias and Figueiredo 2007). Qiao *et al*. (2016a, b, 2019) developed the compressed sensing approach based on the prior of sparsity for identifying the location and time history of nine impact forces from highly incomplete and inaccurate measurements. In SHM, compressed sensing as a powerful tool has been used to extract the dispersion curves of guided wave (Alguri and Harley 2016, Xu *et al*. 2018). Considering the sparsity of guided wave in the wavenumber space, Harley (2016) combined sparse reconstruction algorithms with physic-based wave propagation model for predicting wave behavior in glass-fiber reinforced polymer composite plates without considering boundary reflections. However, many applications benefit from the knowledge of reflections. Furthermore, Alguri and Harlely (2016) proposed a dictionary learning method for building a predictive model of guided wave, which can reconstruct the reflected wave from the geometric boundary and was numerically validated in an aluminum plate.

Currently, some studies are about how compressed sensing can be extended to guided wavefield reconstruction. Based on the sparsity of the wavefield in wavenumber-frequency space and the prior of dispersion property, Mesnil and Ruzzene (2016) reconstructed the guided wavefield of a composite panel from sparse measurements using compressed sensing. In this case, the wavefield measurement error as well as the dispersion relation should be known a priori. Meanwhile, the reflected wave from geometric boundary is ignored and the reconstruction quality is highly sensitive to the precision of the dispersion relation (Yang *et al*. 2018). These approaches that rely on a priori of guided wave velocity and dispersion may not be realistic in practical scenarios, because the wave velocity expressed in an arbitrary structure is generally unknown. The success of guided wavefield sparse reconstruction lies on three factors, i.e., the existence of a sparsifying transform, a favorable random undersampling scheme and a sparsity-promoting recovery method. The undersampling scheme determines the measurement matrix of compressed sensing that should follow the restricted isometry property. Motivated by empirical observations in the seismic community, Hennenfent and Herrmann (2008) employed the jittered undersampling scheme as the measurement matrix of compressed sensing for controlling the maximum gap size of wavefield measurement. Synthetic and real seismic data indicate that the jittered undersampling scheme has a higher accuracy than the regular undersampling scheme in wavefield reconstruction (Hennenfent and Herrmann 2008). To reduce the acquisition time of SLDV for measuring wavefield, Di Ianni *et al*. (2015) used the jittered sampling scheme based on compressed sensing to minimize the number of points, and the SPGL1 algorithm was used to solve the compressed sensing model. Experimental results of an aluminum plate and a glass-fiber-reinforced polymer plate show that the proposed approach could recovery the guided wavefield using less than 34% of the original sampling grid (Di Ianni *et al*. 2015).

In this paper, a wavefield sparse reconstruction method in conjunction with compressive sensing and sparse representation is developed to recovery the full guided wavefield from highly incomplete measurements. Different from the previous research, this work includes: (1) the approach requires only limited measurements and makes no assumption about the physics model; (2) the gradient projection as a convex optimization being computationally faster than competing methods is applied to solve the compressed sensing model of wavefield sparse reconstruction; (3) three undersampling schemes including the regular, random and jittered undersampling schemes are evaluated in a statistical context; and (4) a quantified mapping relation between the sparsity ratio and the recovery error on a special interval is first found in terms of statistics.

2. General description of guided wavefield sparse reconstruction

This section will focus on the compressed sensing model of wavefield sparse reconstruction based on wave propagation and its spatial sparsity in transforming domain. Three undersampling schemes are selected as the measurement matrices of CS model, including the regular, random and jittered schemes.

2.1 Wave propagation model

The guided wave propagation between any two points in a plate can be analytically expressed by their Green's functions. For infinite plates with a single wave source, wave response $y(t)$ at a certain point may be modeled as convolution integral of the excitation source $v_s(t)$ with the Green's function $h(t)$ in the time domain (Sohn *et al*. 2011)

$$y_m(t) = v_s(t) \otimes h_{m,s}(t) = \int_0^t h(t-\tau) v_s(\tau) d\tau \qquad (1)$$

where the symbol $\otimes$ denotes the convolution operation and τ is the time delayed operation satisfying $t \geq \tau$. Eq. (1) describes a forward problem that does not consider the wave propagation reflected from the damage and the geometric boundary, in which the response $y_m(t)$ at arbitrary point is calculated from the corresponding Green's function $h_{m,s}(t)$ and the excitation source $v_s(t)$. Furthermore, the convolution in Eq. (1) can be rewritten in the frequency domain

$$y_m(f) = v_s(f) h_{m,s}(f) = v_s(f) \frac{exp(-ik(f) d_{m,s})}{\sqrt{d_{m,s}}} \qquad (2)$$

where $d_{m,s}$ is the distance between the wave source and the observation point, $k(f)$ is the wavenumber of the mode of interest. Note that Eq. (2) assumes that the plate is sufficiently large so that the reflected wave from the edge can be gated out in the time domain. If multiple-source scenarios are considered, including the reflected waves from damages and geometric boundaries, Eq. (2) can be reformulated as

$$y_m(f) = \sum_{s=1}^{S} v_s(f) h_{m,s}(f) \qquad (3)$$

where *S* is the number of excitation sources. Clearly, guided waves are expressed as a summation of multiple responses.

In this work, the full guided wavefield is reconstructed from limited measurements in the spatial domain rather than in the time domain, and the reconstruction accuracy with respect to the reduction ratio is studied. For a given snapshot of guided wavefield, the general undersampling model in space can be expressed as

$$\boldsymbol{y}_m = \boldsymbol{W} \boldsymbol{y}_n \qquad (4)$$

where the vector $\boldsymbol{y}_m \in \mathbb{R}^m$ denotes the undersampling wavefield data that can be measured typically by a scanning laser Doppler vibrometer; the vector $\boldsymbol{y}_n \in \mathbb{R}^n$ denotes the unknown full wavefield data to reconstruct; *n* is the number of samples which should be acquired to respect the Nyquist sampling theory (i.e., the full-resolution sampling grid); the matrix $\boldsymbol{W} \in \mathbb{R}^{m \times n}$ presents the undersampling operator also named the measurement matrix in CS theory. Each element of $\boldsymbol{W}$ is either zero or one. Eq. (4) makes a high dimension of the full wavefield reduce into a low dimension of the observed wavefield. That is to say, according to the special undersampling operator, the number of measurements *m* is downsampled from the number of full wavefield points *n*. In this case, each row of $\boldsymbol{W}$ can be matched to an individual sensor. The measurement mechanism in Eq. (4) substitutes the traditional Nyquist-based signal collection schemes.

Obviously, if $\boldsymbol{W}$ is an identity matrix, i.e., $\boldsymbol{W} = \boldsymbol{I}$, the sampling process will keep all the points of the full wavefield in the spatial domain. Here, it is assumed that the number of linear measurements *m* is much less than the number of unknown variables *n*, i.e., $n \gg m$. The linear operator $\boldsymbol{W}$ represents an underdetermined mapping from $\boldsymbol{y}_n$ to $\boldsymbol{y}_m$, meaning that Eq. (4) is a severely underdetermined inverse problem. By assuming that the SLDV measurements are almost ideally point-like, the undersampling matrix $\boldsymbol{W}$ is given by the Dirac (identity) basis in which the rows corresponding to *n* - *m* locations are removed from the identity matrix. Furthermore, $\boldsymbol{W} \in \mathbb{R}^{m \times n}$ can be regarded as a truncated identity matrix. Since $\boldsymbol{W}$ is underdetermined, the traditional methods based on least squares methods for solving Eq. (4) end up with infinite solutions. Such limitations can only be overcome with further assumptions imposed.

2.2 Undersampling schemes in space

The design of the undersampling scheme is the most challenging factor for reconstructing guided wavefield. The purpose of designing a measurement matrix is to acquire limited data $\boldsymbol{y}_m$ and then is to guarantee the accurate recovery of the dense data $\boldsymbol{y}_n$. In this section, three undersampling schemes are discussed, including regular, random and jittered schemes. If the undersampling matrix $\boldsymbol{W}$ corresponds to a regular scheme, i.e., data spatially downsampled below the Nyquist sampling rate, the measured points of wavefield along one or two spatial coordinates are evenly distributed over the surface of the structure. For the regular undersampling without randomization, the sampling locations (x_1, x_2) along horizontal and vertical directions on the plate can be defined by

$$\begin{aligned} x_1(i) &= i\Delta; \qquad i = 1,2,\ldots,\frac{Row}{\Delta} \\ x_2(j) &= j\Delta; \qquad j = 1,2,\ldots,\frac{Com}{\Delta} \end{aligned} \qquad (5)$$

where *Row* and *Com* denotes the size of dense grid along horizontal and vertical directions, respectively; the undersampling factor Δ that determines the interval size of the points along horizontal and vertical directions is taken to be $\Delta = 2, 3, \ldots$. The regular undersampling scheme may fail to work because the reconstruction approach cannot efficiently discriminate the original spectrum from its severe aliasing. On the contrary, the random undersampling scheme according to a discrete uniform distribution spreads the energy of the spectral leakage across the Fourier domain, turning coherent aliases into harmless incoherent random noise.

In the approach presented in this article, the number of scan points acquired in a standard laser vibrometer acquisition is decreased by using two different random undersampling techniques. As for the first random undersampling according to a discrete uniform distribution, each point of the wavefield is equally likely to be sampled over the structure.

$$\begin{aligned} x_1(i) &= \varepsilon_i; \qquad i = 1,2,\ldots,\frac{Row}{\Delta} \\ x_2(j) &= \varepsilon_j; \qquad j = 1,2,\ldots,\frac{Com}{\Delta} \end{aligned} \qquad (6)$$

where the discrete random variables ε_i and ε_j are integers independently and identically distributed, according to a uniform distribution on the interval $[1, Row/\Delta]$ and $[1, Com/\Delta]$, respectively. Candes and Romberg' work (2007) showed that taking random measurements is in some sense an optimal strategy for reducing the number of measurements. Consequently, the random undersampling scheme has no control on the size of the maximum gap. Within the field of CS, significant advances have been made regarding the main ingredients that go into the design of an undersampling scheme that favors sparsity-promoting recovery.

A practical requirement of wavefield reconstruction is to control the maximum gap size. Jittered undersampling differentiates itself from random undersampling according to a discrete uniform distribution, which creates favorable recovery conditions by controlling the maximum gap in acquired data (Hennenfent and Herrmann 2008). The basic idea of the jittered undersampling is to regularly decimate the interpolation grid and subsequently perturb the coarse-grid sample points on the fine grid. This means that one measurement is randomly selected within each cell of a regular grid defined in the region of interest. Jittered sampling locations (x_1, x_2) along horizontal and vertical directions on the plane of the plate may be defined by

$$\begin{aligned} x_1(i) &= (i-1)\Delta + \varepsilon_i; \qquad i = 1,2,\ldots,\frac{Row}{\Delta} \\ x_2(j) &= (j-1)\Delta + \varepsilon_j; \qquad j = 1,2,\ldots,\frac{Com}{\Delta} \end{aligned} \tag{7}$$

where the discrete random variables ε_i and ε_j are integers independently and identically distributed, according to a uniform distribution on the interval $[1, \Delta]$. The jittered undersampling factor Δ that determines the size of the perturbation around the coarse regular grid is taken to be $\Delta = 2, 3, \ldots$. It is also assumed that the size n of the interpolation grid is a multiple of Δ^2, so that the number of measured points $m = n/\Delta^2$ is an integer.

Therefore, the elements of the corresponding sampling matrix $\boldsymbol{W}$ are given by

$$\boldsymbol{W}(i,j) = \begin{cases} 1, & \text{if selected} \\ 0, & \text{otherwize} \end{cases} \tag{8}$$

For the jittered undersampling, the maximum gap size cannot exceed 3Δ along two directions; for regular undersampling, all the gaps are of size $\Delta - 1$; for the random undersampling according to a discrete uniform distribution, the maximum gap size is the length of row or column. The random undersampling schemes according to a discrete uniform distribution creates favorable recovery conditions for a reconstruction procedure. Note that the jittered undersampling shares the benefits of the random undersampling.

2.3 Compressed sensing model

The sampled guided wavefield is typically irregularly or coarsely sampled along one or two spatial coordinates and needs to be interpolated before being processed. Generally, the recovery problem of the underdetermined system is ill-posed and permits infinite solutions. Such a limitation can be overcome if further assumptions are applied. In the theoretical framework of compressed sensing, a signal can be recovered exactly from severely undersampled data provided that (1) incoherence: the artifacts introduced by undersampling look like incoherent random noise in sparsifying domain, (2) sparsity: the signal exhibits sparsity in a known transform domain, and (3) solver: a data-consistent sparsity-promoting procedure is used for the recovery (Candes and Romberg 2007). Incoherence is related to the idea that the elements of the sparsifying basis are poorly correlated with the sampling functions. Clearly, the random and jittered undersampling schemes described in previous subsection follows the first principle of compressive sampling.

As mentioned before, CS relies on a sparsifying transform for the recovered signal and uses the sparsity prior to compensate for the undersampling loss during the recovery process. Sparsity expresses the idea that a signal can be represented by a small number of coefficients when expressed in terms of a proper basis. The original signal may not be sparse but its expansion is sparse in the special basis space. Although the actual signal is not exactly sparse, if the elements of the coefficient vector decay exponentially in absolute value, the signal is still compressible by solving the following sparstiy-promoting problem. Mathematically, suppose that at a given time the wavefield data of the dense grid over the surface of the plate $\boldsymbol{y}_n$ is sufficiently sparse in some known transform Φ such that

$$\boldsymbol{y}_n = \Phi \boldsymbol{x} \tag{9}$$

where the transformation matrix $\Phi \in \mathbb{R}^{n \times n}$ is a dictionary matrix constructed by the basis functions. The column of Φ is the discrete waveform of the basis function, known as an atom of the dictionary. $\boldsymbol{x} \in \mathbb{R}^n$ is the coefficient vector of sparse representation, i.e., $\boldsymbol{x}$ has few nonzero entries. The selected dictionary composed of basis functions produces the sparse representation of the considered wavefield data.

A variety of dictionaries have been developed for representing signals. These dictionaries can be based on an analytic formulation such as Fourier, wavelets, or Gabor atoms (Qiao *et al*. 2015, b). Fourier bases are consequently good candidates for the constructing the sparsifying dictionary in the CS recovery procedure. In this paper, the sparsifying transform is defined as the discrete Fourier transform. However, because of its implicit periodicity, the fast Fourier transform (FFT) algorithm may cause reconstruction artifacts (Qiao *et al*. 2015). A way of avoiding this unwanted outcome is to work on the discrete cosine transform (DCT) of the original domain, in place of the discrete Fourier transform, without penalty on redundancy or computational complexity. That is to say that Φ in Eq. (9) presents the inverse discrete cosine transformation. In the strict sense, DCT provides the compressible representation of wavefield data rather than a sparse representation. The sparsity of the wavefield data means that most of the wavefield energy is captured by a few significant coefficients in Fourier domain.

Subsequently, substituting Eq. (9) into Eq. (4), we can get the following formula

$$\boldsymbol{y}_m = \boldsymbol{W\Phi x} = \boldsymbol{Ax} \tag{10}$$

where $\boldsymbol{A} \in \mathbb{R}^{m\times n}$ is called the sensing matrix in terms of CS. We focus on a severely underdetermined system of linear equations. In practical applications, measurements are always contaminated by noise

$$\boldsymbol{y}_m = \boldsymbol{Ax} + \eta \tag{11}$$

where η is the noise term. The target of Eq. (11) is to estimate the vector of the sparse representation coefficients $\boldsymbol{x}$ that provide the optimal recovery of the full wavefield. As a result, the sparsity of $\boldsymbol{x}$ can be used to overcome the singular nature of $\boldsymbol{A}$ when reconstructing $\boldsymbol{y}_n$ from $\boldsymbol{y}_m$. The governing equation describes a forward problem, in which sparse measurements of the system $\boldsymbol{y}_m$ are the product of the sparse representation vector $\boldsymbol{x}$ and the sensing matrix $\mathbf{A}$. In contrast, given $\boldsymbol{y}_m$ and $\boldsymbol{A}$, solving $\boldsymbol{x}$ in Eq. (11) is an inverse problem of an severely underdetermined system.

A convex unconstrained optimization version based on l_1-norm penalty is given by the following sparsity model

$$\min_{x} \frac{1}{2}\|\boldsymbol{y}_m - \boldsymbol{Ax}\|_2^2 + \lambda\|\boldsymbol{x}\|_1 \tag{12}$$

where $\|\boldsymbol{x}\|_1 = \sum_{i=1}^{n}|x_i|$ denotes the l_1-norm of the coefficient vector $\boldsymbol{x}$, and λ is the regularization parameter that establishes a fair balance between the residual and the sparsity of the unknown representation coefficients. The regularization penalty term $\|\boldsymbol{x}\|_1$ encourages small components of the coefficient vector $\boldsymbol{x}$ to become zeros, and thus it can promote sparse solutions. Among all possible solutions of the severely underdetermined equation (Eq. (11)), the optimization problem of Eq. (12) finds the sparsest possible solution that explains the data. The l_1-norm regularization problem of Eq. (12) is convex and can be solved by many classical optimization algorithms (Bioucas-Dias and Figueiredo 2007, Figueiredo *et al.* 2007, Tropp and Wright 2010). The uniqueness of the sparse solution of Eq. (12) has been validated in (Candes and Wakin 2008, Donoho 2006) under the special condition.

According to the compressed sensing theory, if Eq. (12) exits the sparsest solution, the following two conditions should be satisfied: (1) the coefficient vector $\boldsymbol{x}$ is sufficiently sparse; (2) the elements of the undersampling operator are incoherent. The first condition of sparsity requires that the energy of $\boldsymbol{x}$ is well concentrated in the sparsifying domain. The second condition of incoherent random undersampling involves the study of the sparsifying transform $\boldsymbol{\Phi}$ in conjunction with the undersampling operator $\boldsymbol{W}$. When the second condition is not satisfied, sparsity alone is no longer an effective prior to solve the recovery problem. Meanwhile, the second condition provides a fundamental insight in choosing undersampling schemes that favor recovery by sparsity-promoting inversion.

The application of l_1-norm penalty in Eq. (12) requires that the sensing matrix $\boldsymbol{A}$ verifies the restricted isometry property (RIP) with a constant δ_s smaller than unity (Donoho 2006)

$$(1-\delta_s)\|\boldsymbol{y}\|_2^2 \le \|\boldsymbol{A}_s\boldsymbol{x}\|_2^2 \le (1+\delta_s)\|\boldsymbol{y}\|_2^2 \tag{13}$$

In practice this requirement is often replaced by ensuring that matrices $\boldsymbol{W}$ and $\boldsymbol{\Phi}$ are incoherent (Candes and Romberg 2007, Perelli *et al.* 2013). It is mathematically verified by checking that the coherence, i.e., the maximum value of the scalar product between all the columns of the matrix $\boldsymbol{A}$, is smaller than a constant defined in (Candes and Romberg 2007), meaning that the matrix $\boldsymbol{A}$ is nearly orthonormal. This condition helps ensure that sparse recovery algorithms satisfy the RIP to accurately recover the sparse representation with a sufficient number of measurements. It is also worth noting that the inverse Fourier transforms operator $\boldsymbol{\Phi}$ is maximally incoherent with the sampling matrix $\boldsymbol{W}$. Furthermore, if $\boldsymbol{y}_n$ is sparse in certain a transform domain and $\boldsymbol{A}$satisfies the RIP, there exists approaches that can uniquely reconstruct $\boldsymbol{y}_n$ from the limited measurements $\boldsymbol{y}_m$. We randomly sample in space so that each measurement provides unique spatial information about guided wavefield.

3. The gradient projection approach for guided wavefield sparse reconstruction

Many convex optimization solvers often grouped into interior-point methods (Kim *et al.* 2007), iterative shrinkage/thresholding algorithms (Bioucas-Dias and Figueiredo 2007, Beck and Teboulle 2009) and projected gradient methods (Figueiredo *et al.* 2007), have been specifically adapted to the sparse reconstruction model for signal/image processing. In many cases, these algorithms are convex, computationally efficient, and robust. Different from other convex solvers, the iterative shrinkage/ thresholding algorithms and the gradient projection algorithms involve only matrix-vector products and do not involve expensive operations such as matrix factorization. Note that the iterative shrinkage/thresholding algorithms is applicable for the sparse deconvolution problem rather than the compressed sensing model of the underdetermined system (Qiao *et al.* 2019, Figueiredo *et al.* 2007). This study focuses on an improved gradient projection method for solving the compressed sensing model of guided wavefield sparse reconstruction in which there are fewer equations than unknowns. This section provides an overview of how the compressed sensing model of guided wavefield is implemented using the improved gradient projection algorithm.

The gradient projection approach for sparse reconstruction has been applied to compressed sensing and other inverse problems (Figueiredo *et al.* 2007). Here, the gradient projection approach based on the l_1-minimizer is selected for solving the CS problem due to its robustness in the presence of measurement noise. In order to employ the gradient projection approach for solving the severely underdetermined problem of guided wavefield sparse reconstruction, Eq. (12) should be formulated as a quadratic program. Firstly, one can split the sparse representation coefficient vector $\boldsymbol{x}$ into the positive and negative parts as follows

$$\boldsymbol{x} = \boldsymbol{u} - \boldsymbol{v}, \qquad \boldsymbol{u} \geq 0, \qquad \boldsymbol{v} \geq 0 \tag{14}$$

where the elements of $\boldsymbol{u}$ and $\boldsymbol{v}$ are defined as $u_i = (x_i)_+$ and $v_i = (-x_i)_+$ for i = 1, 2 ,…, n. $(x)_+ = max\{0, x\}$ denotes the positive-part operator. Thus, the sparsity-induced term in Eq. (12) can be expressed as $\|\boldsymbol{x}\|_1 = \mathbf{1}_n^T\boldsymbol{u} + \mathbf{1}_n^T\boldsymbol{v}$, where the vector $\mathbf{1}_n = [1,1,\ldots,1]^T$ is composed of n ones. Therefore, Eq. (12) can be rewritten as a bound-constrained quadratic program

$$\begin{aligned} &\underset{\boldsymbol{u},\boldsymbol{v}}{min}\frac{1}{2}\|\boldsymbol{y}_m - \boldsymbol{A}(\boldsymbol{u}-\boldsymbol{v})\|_2^2 + \lambda(\mathbf{1}_n^T\boldsymbol{u} + \mathbf{1}_n^T\boldsymbol{v}); \\ &\text{subject to } \mathbf{u} \geq 0, \mathbf{v} \geq 0 \end{aligned} \tag{15}$$

Furthermore, Eq. (15) can be rewritten as a standard quadratic program

$$\underset{\boldsymbol{z}}{min}G(\boldsymbol{z}) = \frac{1}{2}\boldsymbol{z}^T\boldsymbol{B}\boldsymbol{z} + \boldsymbol{c}^T\boldsymbol{z}; \qquad \boldsymbol{z} \geq 0 \tag{16}$$

where

$$\begin{aligned} &\boldsymbol{B} = \begin{bmatrix} \boldsymbol{A}^T\boldsymbol{A} & -\boldsymbol{A}^T\boldsymbol{A} \\ -\boldsymbol{A}^T\boldsymbol{A} & \boldsymbol{A}^T\boldsymbol{A} \end{bmatrix}, \qquad &&\mathbf{z} = \begin{bmatrix} \boldsymbol{u} \\ \boldsymbol{v} \end{bmatrix}, \\ &\boldsymbol{c} = \lambda\mathbf{1}_{2n} + \begin{bmatrix} -\boldsymbol{b} \\ \boldsymbol{b} \end{bmatrix}, &&\boldsymbol{b} = \boldsymbol{A}^T\boldsymbol{y}_m \end{aligned} \tag{17}$$

The gradient of the objective function Eq. (16) is $\nabla G(\boldsymbol{x}) = \boldsymbol{B}\boldsymbol{z} + \boldsymbol{c}$. It can be seen that compared with the original problem described in Eq. (12), the dimension of Eq. (16) is enlarged twice, i.e., $\boldsymbol{z} \in \mathbb{R}^{2n}$. Indeed, the matrix-vector operation involving $\boldsymbol{B}$ can be performed more efficiently by virtue of its special structure.

As part of the gradient projection approach of an iterative scheme, the target is to find the solution $\boldsymbol{z}_{k+1}$ at iteration $k+1$ from the solution $\boldsymbol{z}_k$ at iteration k by the following formula

$$\boldsymbol{z}_{k+1} = \boldsymbol{z}_k + \tau_k\boldsymbol{\delta}_k \tag{18}$$

Because the objective function of Eq. (16) is quadratic, the scalar $\tau_k \in [0,1]$ as the line search parameter can be determined simply by the closed-form formula

$$\tau_k = \text{mid}\left\{0, \frac{(\boldsymbol{\delta}_k)^T\nabla G(\boldsymbol{z}_k)}{(\boldsymbol{\delta}_k)^T\boldsymbol{B}\boldsymbol{\delta}_k}, 1\right\} \tag{19}$$

Note that if $(\boldsymbol{\delta}_k)^T\boldsymbol{B}\boldsymbol{\delta}_k = 0$, the scalar is set $\tau_k = 1$, and $\boldsymbol{\delta}_k$ is determined at each iteration as

$$\boldsymbol{\delta}_k = (\boldsymbol{z}_k - \alpha_k\nabla G(\boldsymbol{z}_k))_+ - \boldsymbol{z}_k \tag{20}$$

where the scalar parameter α_k is selected on the interval $[\alpha max_{min}$ by a closed-form formula

$$\alpha_k = \text{mid}\left\{\alpha\frac{\|\boldsymbol{\delta}_{k-1}\|_2^2}{(\boldsymbol{\delta}_k)^T\boldsymbol{B}\boldsymbol{\delta}_{k_{max_{min}}}}\right\} \tag{21}$$

It should be emphasized that the proposed approach for guided wavefield sparse reconstruction does not require matrix factorizations and only involves vector operations as well as matrix-vector multiplications at each iteration.

The convergence speed of the convex optimization approaches for solving Eq. (16) benefits from a good starting point of the regularization parameter. That suggests that the speed of the gradient projection may become slow for small regularization parameters λ . Numerous experiments (Wright *et al.* 2009, Qiao *et al.* 2016b) demonstrated that the convergence of the gradient projection method and other convex optimization methods becomes slow if λ is small. If there is initially a large λ, and then decrease λ gradually to the desired $\bar{\lambda}$, it is usually much more efficiently to achieve a sparse solution. Such an accelerating strategy for dealing with the regularization parameter in sparse reconstruction methods is called continuation (Kim *et al.* 2007). The continuation scheme is shown to considerably speed up the iterative algorithm, leading to a converged solution in fewer iterations. In such a case, the gradient projection can be embedded in a continuation heuristic to accelerate its iteration. Naturally, the primary issue of continuation is how to construct a decreasing sequence of λ that yields a fast convergence rate. In this case, a decreasing sequence with respect to each iteration k, $\lambda_0 > \lambda_1 \cdots > \lambda_k \cdots > \bar{\lambda}$, is determined in advance, where $\bar{\lambda}$ denotes the target regularization parameter. Using this continuation strategy, the intermediate solution with λ_{k-1} is chosen as the initial estimate for the next iteration with λ_k. In this work, the initial regularization parameter from a cold start is set as the largest value of $\lambda = 0.8\|\boldsymbol{A}^T\boldsymbol{y}_m\|_\infty$, then decreased by a constant factor in 10 steps until the target value of $\lambda = 0.001\|\boldsymbol{A}^T\boldsymbol{y}_m\|_\infty$ is achieved. Experiments in the following section demonstrate that these parameters performance well in all cases.

For an iterative process, choosing a good stopping criterion is important to timely stop an iteration when $\boldsymbol{z}_k$ becomes close to the optimum. The objective function $G(\boldsymbol{z})$ is reasonably close to an optimal one $G(\boldsymbol{z}^*)$. Here the relative change of the objective function (Eq. (16)) between two successive iterations is selected as the stopping criterion, defined as

$$\frac{|G(\boldsymbol{z}_{k+1}) - G(\boldsymbol{z}_k)|}{G(\boldsymbol{z}_{k+1})} \leq tol \tag{22}$$

where tol is a small tolerance parameter, empirically set as $\varepsilon = 10^{-6}$ (Qiao *et al.* 2019). It means that once the relative change is less than or equal to an acceptable relative tolerance tol, the iteration process will be stopped.

4. Experimental verification

In this section, a series of controlled experiments on an aluminum plate are conducted to verify the effectiveness and reliability of the sparse reconstruction approach under different excitation frequencies, different undersampling schemes and different undersampling ratios. Three undersampling schemes including regular, random and jittered schemes are compared and their recovery uncertainty is in detail compared. A quantified mapping relation between the undersampling ratio and the recovery error is established with respect to statistical modeling and analysis.

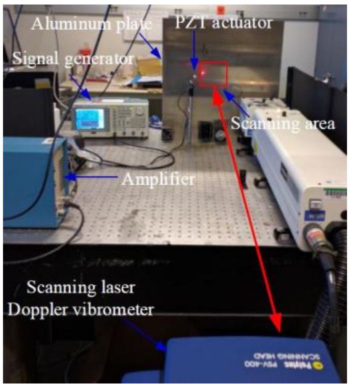

Fig. 1 Experimental set-up for guided wavefield measurement using the scanning laser Doppler vibrometer

4.1 Experiment description

A pristine aluminum plate (6061-T6) with a size of 520×520×3 mm is set up as shown in Fig. 1. In this work, ultrasonic guided waves are generated using a fixed piezoelectric transducer and their responses are measured using a scanning laser Doppler vibrometer. A given inspection region of 50×50 mm on a dense grid of 49×47 (n = 2303 points) equally spaced points is scanned by a Polytec PSV400 SLDV. Neighbor points are approximately separated by 1 mm. The excitation signal of ultrasonic is generated by an arbitrary waveform signal generator and then amplified to 80 Vpp by a power amplifier for exciting the PZT. The excitation function is a 5-cycle Hanning windowed tone burst at two distinct central frequencies of 30 kHz and 50 kHz as shown in Fig. 2. The excitation signal is applied to a round 10-mm-diameter piezoelectric transducer located on the left of the plate away from the scanned region. The guided wavefield data with out-of-plane velocities are measured by SLDV. Each sampling point can be seen as a virtual sensor for recording guided wave signal. The sampling frequency of SLDV is 204.8 kHz. Each point is repeatedly recorded 20 times for averaging purposes to reduce the measurement noise as much as possible. Note that the present reconstruction method allows for some degree of measurement error. The duration of scanning each point is 10 ms with a waiting time of 100 ms between neighbor measurements so that the wavefront of the previous measurement does not interfere with the latter measurement. For measuring guided wavefield by SLDV, it is critical to keep the synchronization between generating the ultrasonic wave by PZT and recording the wavefield by SLDV. Here, the control unit of SLDV can send a pulse trigger signal to both the signal generator and the acquisition process at each scan.

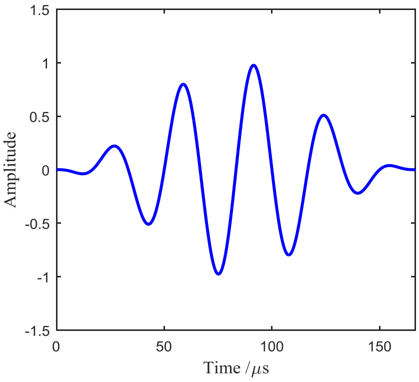

(a) 30 kHz

Fig. 2 Two Hanning-windowed e

Only a subset of scanning measurements are used for the problem formulation, while the entire set of scanning measurements are retained for evaluating the reconstruction accuracy. Wavefield data are reconstructed only on the grid of the measured full wavefield for comparison purposes. To clearly highlight each step of guided wavefield sparse reconstruction using compressed sensing, an overview of the whole procedure is depicted in Fig. 3, including (1) the sampling points in the spatial domain are determined by following an undersampling scheme where the measurement matrix $\boldsymbol{W} \in \mathbb{R}^{m \times n}$ of the compressed sensing model is determined; (2) the limited guided wavefield measurements $\boldsymbol{y}_m \in \mathbb{R}^m$ are recorded by using SLDV; (3) the full wavefield $\boldsymbol{y}_n \in \mathbb{R}^n$ on the dense grid are represented by the discrete cosine functions $\boldsymbol{\Phi} \in \mathbb{R}^{n \times n}$; (4) given $\boldsymbol{y}_m$, $\boldsymbol{W}$ and $\boldsymbol{\Phi}$, one can construct the compressed sensing model in Eq. (12); (5) the gradient projection approach is applied to solved the convex optimization model of compressed sensing, and then the solution of the sparse coefficient vector $\boldsymbol{x} \in \mathbb{R}^n$ is obtained; (6) considering Eq. (9), the guided wavefield $\boldsymbol{y}_n \in \mathbb{R}^n$ is reconstructed; (7) the uncertainty of different undersampling schemes and ratios on reconstruction accuracy are further investigated. Once the ultrasonic guided wave signals are collected over the entire scanning area, they can be post-processed for ultrasonic wavefield sparse reconstruction.

The quality of wavefield sparse reconstruction solution will be quantitatively evaluated by the signal-to-reconstruction error-ratio between the measured and reconstructed wavefields, defined as

$$SNR = 20\,log\left(\frac{\|\boldsymbol{y}_n\|_2}{\|\boldsymbol{y}_n - \tilde{\boldsymbol{y}}_n\|_2}\right) \tag{23}$$

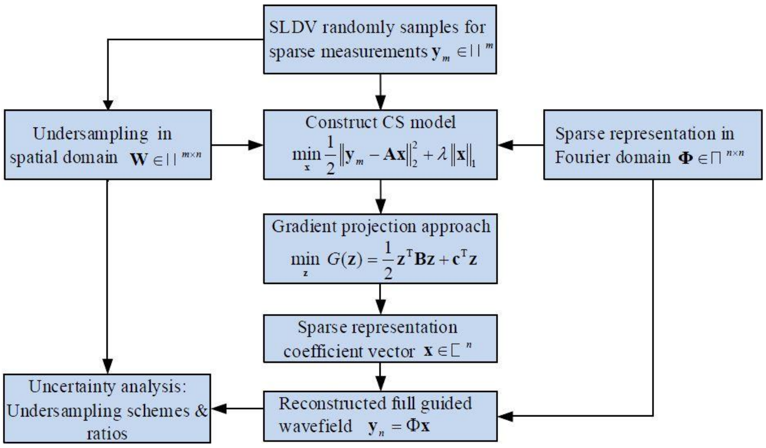

Fig. 3 The flowchart of guided wavefield sparse reconstruction using compressed sensing

where $\boldsymbol{y}_n$ is the measured wavefield signal acquired on the dense grid by SLDV, and $\tilde{\boldsymbol{y}}_n$ is the reconstructed wavefield signal by compressed sensing. The main objective of this work is to evaluate the capability of preserving the informative content of the signal (i.e., high SNR) while reducing the number of acquisition points, because such a reduction implies a parallel reduction of the acquisition time and a more efficient usage of the SLDV equipment. Furthermore, the undersampling ratio of the reconstructed wavefield with respect to Nyquist theorem is defined by

$$Ratio = \frac{m}{n} \times 100\% \tag{24}$$

where *Ratio* expresses the reduction of the number of measurements to acquire with respect to the full capture of the wavefield based on sampling criteria. Therefore, the compression ratio of the reconstructed wavefield can be thought as 1-*Ratio*.

4.2 Wavefield reconstruction using different undersampling schemes

Three undersampling schemes including the random, jittered and regular ones are conducted from a uniform full-resolution grid on a 2-D spatial domain as shown in Fig. 4. The solid red circles correspond to the coarse under-sampling locations $\boldsymbol{y}_m$, which can be sparsely measured by SLDV. The fine grid of blue points denotes the full wavefield $\boldsymbol{y}_n$, which is desired to be reconstructed. The upper panel of Fig. 4 depicts the distribution of 600 undersampling points from 2303 dense points using three different schemes, meaning that one-out-of-four samples are approximately recorded. The lower panel of Fig. 4 depicts the distribution of 272 undersampling points from 2303 dense points using three different schemes, meaning that one-out-of-nine samples are approximately recorded. The size of the measurement matrix $\boldsymbol{W}$ for the compressed

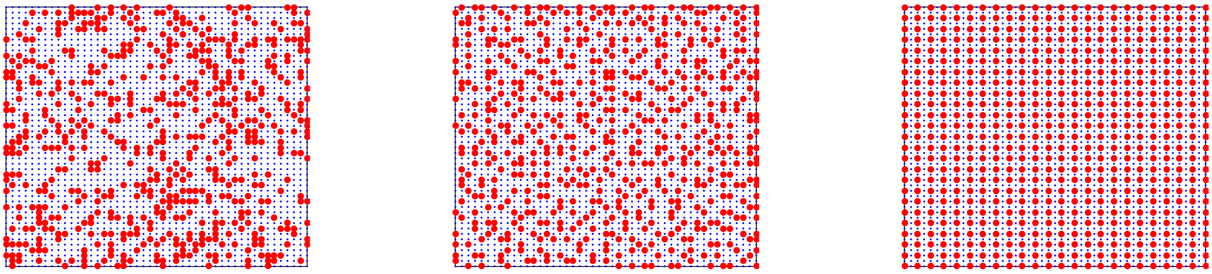

(a) Selected 600 from 2303 dense points using the random scheme

(b) Selected 600 from 2303 dense points using the jittered scheme

(c) Selected 600 from 2303 dense points using the regular scheme

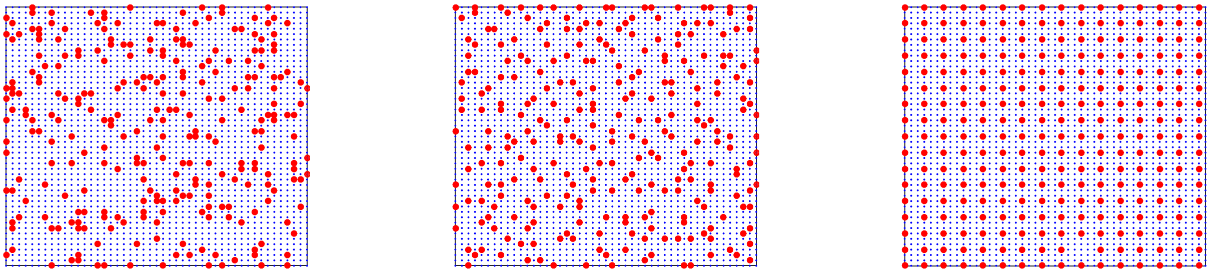

(d) Selected 272 from 2303 dense points using the random scheme

(e) Selected 272 from 2303 dense points using the jittered scheme

(f) Selected 272 from 2303 dense points using the regular scheme

Fig. 4 Three undersampling schemes with different sampling cases sensing model is 600×2303 and 272×2303, corresponding to undersampling ratios 26.05% and 11.81%, respectively. It can be seen from Fig. 4 that the distribution of the undersampling points using the random and jittered schemes according to a discrete uniform distribution is random along horizontal and vertical directions in the spatial domain. On the contrary, the distribution of the undersampling points in Figs. 4 (c) and (f) is even regular aligned along horizontal and vertical directions. Furthermore, compared with the random scheme in Figs. 4(a) and (b), the gap of the neighbor points using the jittered scheme on the grid is smaller.

We focus on the recovery of the missing wavefield from highly incompletely experimental data. Only a fraction of the number of measurements are taken without any prior knowledge of their dispersion relative. Comparisons are made among the reconstruction results of four-fold and nine-fold spatially undersampled data. To evaluate the gradient projection method for solving the compressed sensing model, the wavefield recovery results of two snapshots related to different excitation frequencies, undersampling schemes and ratios are illustrated in Figs. 5-8. Note that the guided wavefields measured by SLDV in Figs. 5 and 7 are directly generated by PZT without boundary reflections; the guided wavefields in Figs. 6 and 8 are mainly reflected from the left boundary of the plate. Two different wavefield snapshots with excitation frequencies 30 kHz and 50 kHz are taken as examples. For instance, Fig. 5 illustrates the sparse reconstruction results of a snapshot (t = 180.66 μs) of the guided wave propaga-

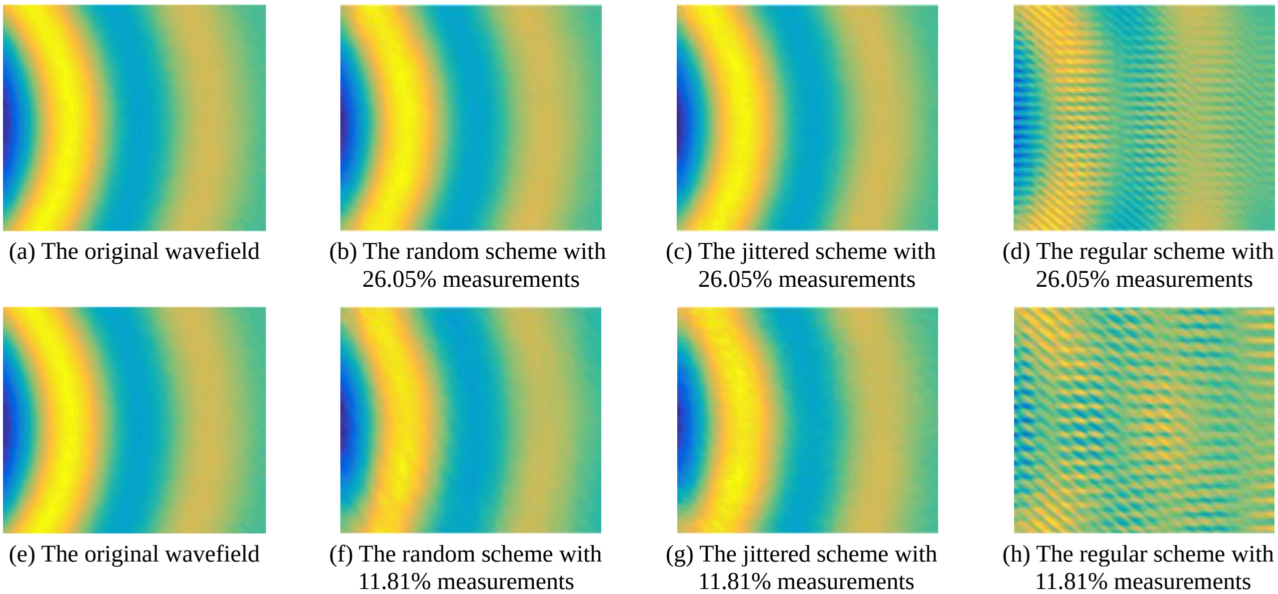
(a) The original wavefield (b) The random scheme with 26.05% measurements (c) The jittered scheme with 26.05% measurements (d) The regular scheme with 26.05% measurements

(e) The original wavefield (f) The random scheme with 11.81% measurements (g) The jittered scheme with 11.81% measurements (h) The regular scheme with 11.81% measurements

Fig. 5 Comparison for reconstructing a wavefield snapshot (t = 180.66 μs) with 30 kHz using different sampling schemes

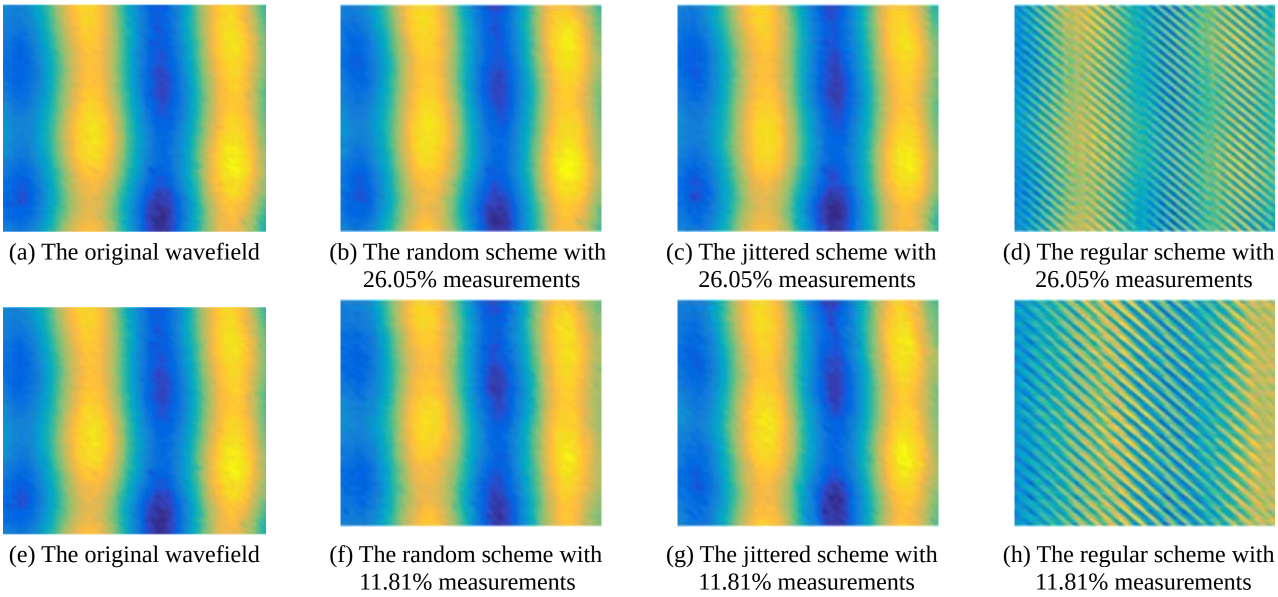
(a) The original wavefield (b) The random scheme with 26.05% measurements (c) The jittered scheme with 26.05% measurements (d) The regular scheme with 26.05% measurements

(e) The original wavefield (f) The random scheme with 11.81% measurements (g) The jittered scheme with 11.81% measurements (h) The regular scheme with 11.81% measurements

Fig. 6 Comparison for reconstructing a wavefield snapshot (t = 400.39 μs) with 30 kHz using different sampling schemes tion at 30 kHz using three undersampling schemes along with two different undersampling ratios. Images of the first column in Fig. 5 as a reference are the original wavefield measured from SLDV and sampled above Nyquist rate along the horizontal and vertical directions. Note that Figs. 5(a) and (e) have the same snapshot at a given time instant. The upper panel of Fig. 5 depicts the results of the snapshot (t = 180.66 μs) from 26.05% measurements using random, jittered and regular schemes. The lower panel of Fig. 5 depicts the results of the snapshot (t = 180.66 μs) from 11.81% measurements using random, jittered and regular schemes. Visually, in Figs. 5(d) and (h), the recovery results of the regularly undersampled wavefield using compressed sensing is severely aliased and unacceptable, no matter what the undersampling ratio is set. The situation is completely different in Figs. 5(b), (c) and (f), (g) for the random and jittered schemes. One can find that no matter the undersampling ratio is set as 26.05% or 11.81%, the reconstructed snapshots using random and jittered schemes have a perfect match with the measured snapshot. Furthermore, it seems that the jittered scheme has a better result than the random scheme. Similarly, for another snapshot (t = 400.39 μs) with 30 kHz, the reconstructed results using random and jittered schemes still have a good match with the measured snapshot as shown in Fig. 6.

To evaluate the performance of the gradient projection approach for reconstructing wavefield with different excitation frequencies, two snapshots with 50 kHz are also reconstructed using three undersampling schemes as shown in Figs. 7 and 8. Compared with the cases with the excitation frequency 30 kHz in Figs. 5 and 6, the wavefields with the excitation frequency 50 kHz in Figs. 7 and 8 include more waves in the same region over the structure. Nevertheless, the reconstructed snapshots using both the random and jittered scheme have a perfect match with the measured one, no matter the undersampling ratio is set as 26.05% or 11.81%. The number of measurement points required for ultrasonic wavefield image is dramatically reduced. The difference between the measured wavefield and the reconstructed wavefield using the random and jittered schemes is visually negligible. It seems that the jittered scheme leads to an improved recovery compared to the random scheme according to a discrete uniform distribution. Conversely, the gradient projection approach of compressed sensing cannot generate the acceptable solution from the regular undersampling scheme. One can conclude that for a given undersampling ratio, both the random and jittered schemes are much more favorable than the regular scheme. Note that the difference in reconstruction quality solely lies in the spatial distribution of the sampled points, and the undersampling ratio as well as the recovery procedure is kept same.

More specifically, in order to compare the effects of three undersampling schemes, the signal-to-reconstruction-error-ratios (SNR) defined in Eq. (23) with excitation frequencies 30 kHz and 50 kHz are quantitatively listed in Tables 1 and 2, respectively. Clearly, the values of SNR for all the cases using the regular scheme are extremely low (less than 3 dB) and unacceptable. For the same snapshot at the same excitation frequency, the reconstructed wavefield using the undersampling ratio 26.05% has much higher SNR than that using the undersampling ratio 11.81%. These experiments illustrate that both random and jittered samplings create favorable results from severely undersampled points, which are much more accurate than those achieved by the simply regular scheme. Furthermore, SNRs of the jittered scheme are slightly higher than those of the random scheme under the same condition. For instance, SNRs of the random and jittered schemes with the excitation frequency 30 kHz at 180.66 μs are respectively 23.01 dB and 25.32 dB. It means that the jittered scheme behaves similarly as the random scheme according to a discrete uniform distribution.

More specifically, in order to compare the effects of three undersampling schemes, the signal-to-reconstruction-error-ratios (SNR) defined in Eq. (23) with excitation

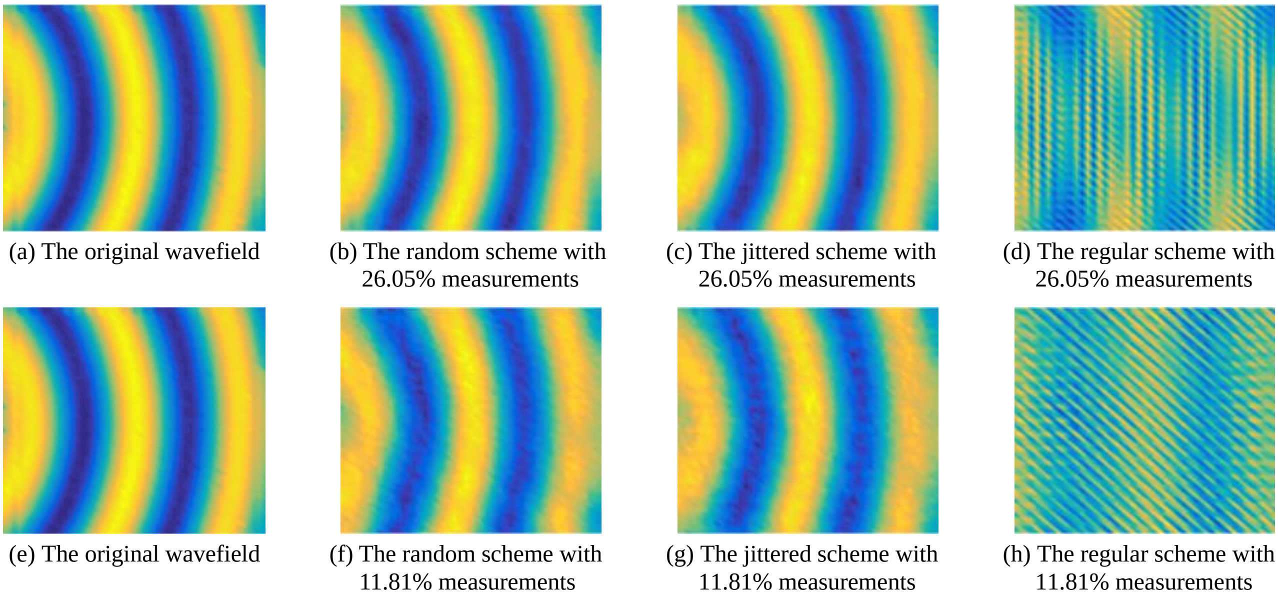
(a) The original wavefield
(b) The random scheme with 26.05% measurements
(c) The jittered scheme with 26.05% measurements
(d) The regular scheme with 26.05% measurements
(e) The original wavefield
(f) The random scheme with 11.81% measurements
(g) The jittered scheme with 11.81% measurements
(h) The regular scheme with 11.81% measurements

Fig. 7 Comparison for reconstructing a wavefield snapshot (t = 190.43 μs) with 50 kHz using different sampling schemes

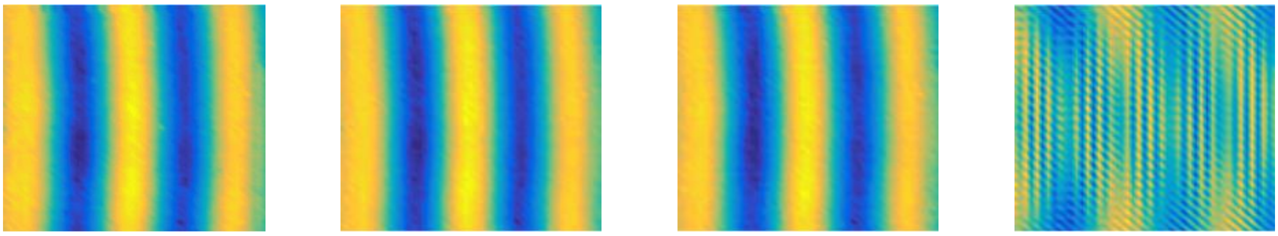

(a) The original wavefield (b) The random scheme with 26.05% measurements (c) The jittered scheme with 26.05% measurements (d) The regular scheme with 26.05% measurements

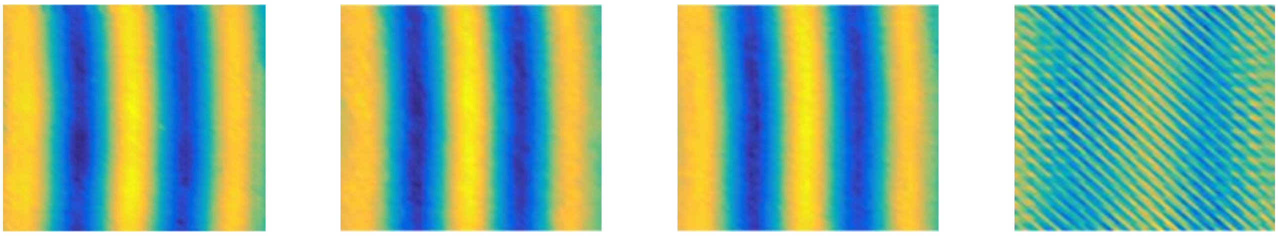

(e) The original wavefield (f) The random scheme with 11.81% measurements (g) The jittered scheme with 11.81% measurements (h) The regular scheme with 11.81% measurements

Fig. 8 Comparison for reconstructing a wavefield snapshot (t = 317.38 μs) with 50 kHz using different sampling schemes

Table 1 SNR of the reconstructed guided wavefield with 30 kHz using three undersampling schemes.

Snapshot /μs	Sampling ratio	Random /dB	Jittered /dB	Regular /dB
180.66	26.05	23.01	25.32	2.62
	11.81	17.86	18.89	-0.75
400.39	26.05	22.48	23.14	-0.10
	11.81	18.53	19.39	0.12

Table 2 SNR of the reconstructed guided wavefield with the excitation frequency 50 kHz using three undersampling schemes

Snapshot /μs	Sampling ratio	Random /dB	Jittered /dB	Regular /dB
190.43	26.05	21.62	22.45	-0.26
	11.81	14.92	16.23	-0.58
317.38	26.05	21.82	21.85	-2.04
	11.81	18.40	18.96	2.38

frequencies 30 kHz and 50 kHz are quantitatively listed in Tables 1 and 2, respectively. Clearly, the values of SNR for all the cases using the regular scheme are extremely low (less than 3 dB) and unacceptable. For the same snapshot at the same excitation frequency, the reconstructed wavefield using the undersampling ratio 26.05% has much higher SNR than that using the undersampling ratio 11.81%. These experiments illustrate that both random and jittered samplings create favorable results from severely undersampled points, which are much more accurate than those achieved by the simply regular scheme. Furthermore, SNRs of the jittered scheme are slightly higher than those of the random scheme under the same condition. For instance, SNRs of the random and jittered schemes with the excitation frequency 30 kHz at 180.66 μs are respectively 23.01 dB and 25.32 dB. It means that the jittered scheme behaves similarly as the random scheme according to a discrete uniform distribution.

Therefore, we can conclude that it is possible, under specific conditions, to exactly recover the original full wavefield from highly incomplete measurements by the gradient projection approach. Thus, the proposed sparse reconstruction technique is able to recover the guided wavefield from only 11.81% of measurements required by Nyquist theorem. In general, the jittered scheme has a slightly higher accuracy than the random scheme. Both random schemes can lead to an accurate reconstruction as good as the dense regular sampling using SLDV. For practical purposes, the former can thus be seen as an alternative undersampling scheme of the latter. Not all sampling schemes for a given undersampling ratio are comparable from a CS perspective. It is quite difficult for the regular scheme to reconstruct the full wavefield from limited data.

4.3 Uncertainty comparison of different undersampling schemes

The previous section illustrates the effectiveness and reliability of the sparse reconstruction approach from highly incomplete data through a single experiment. It has been experimentally demonstrated that the regular scheme always has a bad result. In this section, we will focus on the uncertainty comparison of two random undersampling schemes through a huge number of wavefield sparse reconstruction experiments. Here, the uncertainty is defined as the standard uncertainty that is equal to the standard deviation (Kirkup and Frenkel 2006). Each experiment is randomly repeated 1000 times, while the excitation frequency, the undersampling scheme and the number of sampling points remain unchanged. The sole difference lies in the distribution of the undersampling points in the spatial

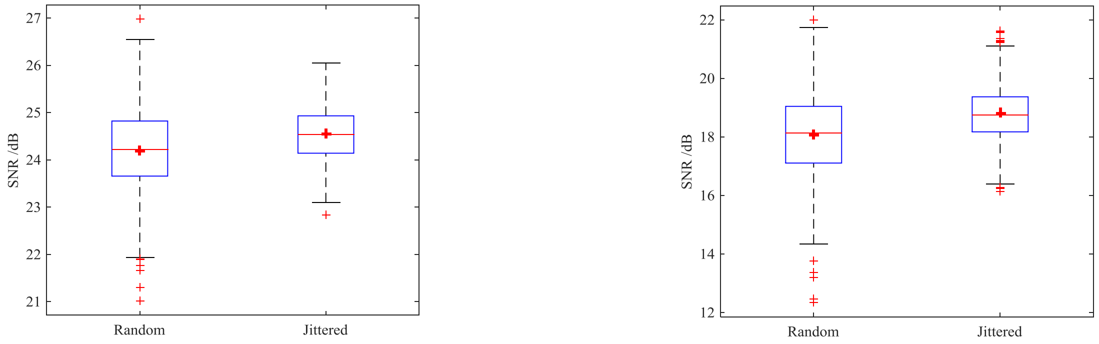

(a) *t* = 180.66 μs with 26.05% measurements (b) *t* = 180.66 μs with 11.81% measurements

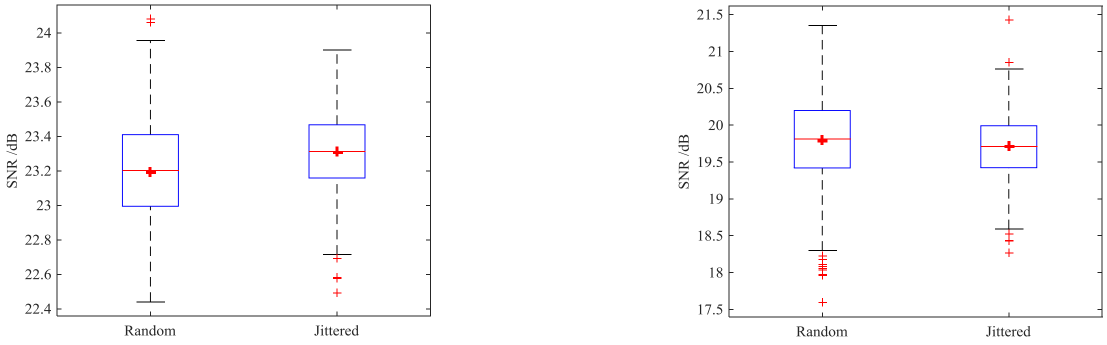

(c) *t* = 400.39 μs with 26.05% measurements (d) *t* = 400.39 μs with 11.81% measurements

Fig. 9 Uncertainty comparison of different sampling schemes with 30 kHz in terms of SNR

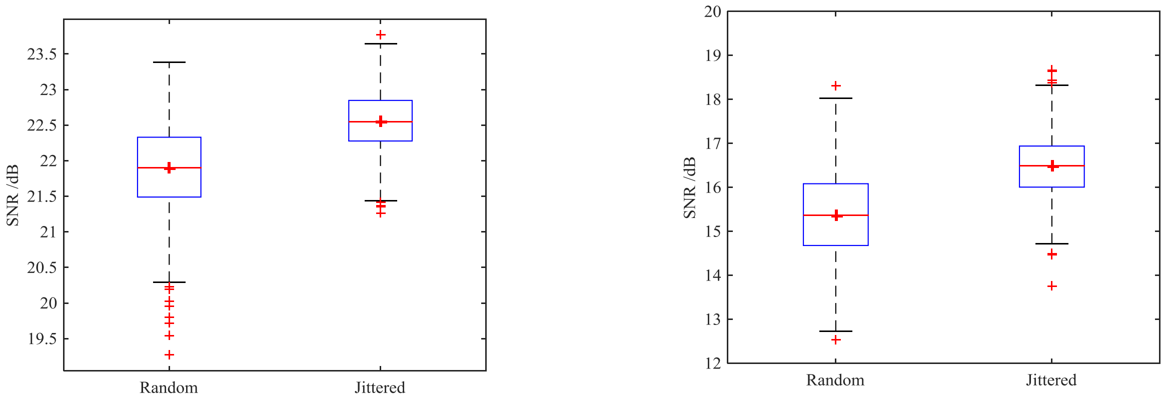

(a) *t* = 190.43 μs with 26.05% measurements (b) *t* = 190.43 μs with 11.81% measurements

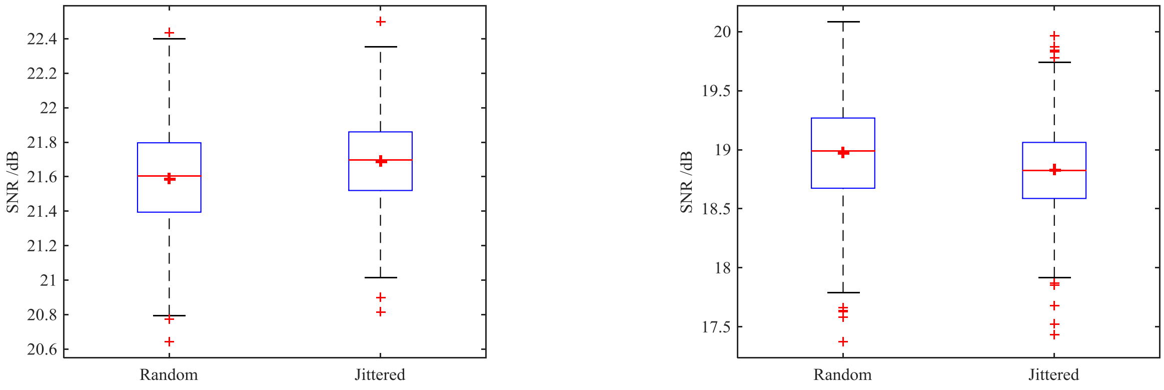

(c) *t* = 317.38 μs with 26.05% measurements (d) *t* = 317.38 μs with 11.81% measurements

Fig. 10 Uncertainty comparison of different sampling schemes with 50 kHz in terms of SNR

Table 3 Uncertainty comparison of different sampling schemes at 30 kHz in terms of SNR

Sampling scheme		Random undersampling /dB		Jittered undersampling /dB	
Snapshot /μs	Sampling ratio	Mean of SNR	Std of SNR	Mean of SNR	Std of SNR
180.66	26.05	24.19	0.86	24.55	0.54
	11.81	18.05	1.44	18.79	0.90
400.39	26.05	23.19	0.29	23.31	0.23
	11.81	19.79	0.60	19.71	0.42

Table 4 Uncertainty comparison of different sampling schemes at 50 kHz in terms of SNR

Sampling scheme		Random undersampling /dB		Jittered undersampling /dB	
Snapshot /μs	Sampling ratio	Mean of SNR	Std of SNR	Mean of SNR	Std of SNR
190.43	26.05	21.88	0.60	22.54	0.41
	11.81	15.35	1.03	16.47	0.68
317.38	26.05	21.59	0.29	21.69	0.24
	11.81	18.97	0.43	18.83	0.35

domain. The SNR of the reconstructed wavefield is again used to quantify the quality of the reconstruction procedure as shown in Figs. 9 and 10. In Fig. 9, the first and second columns illustrate the box plots of SNRs of the reconstructed wavefield at 30 kHz, which correspond to the undersampling ratios 26.05% and 11.81%, respectively. The central mark, i.e., the red line, presents the median of 1000 SNRs, the edges of the box are the 25th and 75th percentiles, the whiskers present the most extreme datapoints. The SNRs outside of the whiskers are considered to be outliers and are plotted individually by thin "+". Meanwhile, the mean of 1000 SNRs is also depicted and symbolized by thick "+". It can be seen from Figs. 9 and 10 that the median and mean values of 1000 SNRs are quite close. There exit the considerable overlap between the distributions of SNRs of the random and jittered schemes in term of statistics.

Compared with the random scheme, the intervals of both the box edges and the whiskers using the jittered scheme in Figs. 9 and 10 are smaller. It can be further found in Tables 3 and 4 that the standard deviations (i.e., namely the standard uncertainty) of SNRs of all the experiments are less than 1.5 dB; the standard deviations of jittered undersampling are smaller than those of random undersampling; the mean SNRs of jittered undersampling are commonly higher than those of random undersampling. Meanwhile, we can see from Figs. 9(d) and 10(d) that the mean SNRs of jittered undersampling are slightly lower than those of random undersampling, and its uncertainty in term of SNR is also smaller. Therefore, one can conclude from the uncertainty comparison that the wavefield sparse reconstruction approach based on both random and jittered schemes can achieve high SNRs. In general, the jittered scheme that produces a more uniform distribution, has a slightly better recovery than the random scheme in terms of statistics. The standard uncertainty of the jittered scheme is always smaller than that of the random scheme under the same condition. It is worth to mention that it is difficult to compare random and jittered schemes in limited experiments due to the overlap of probability distribution.

4.4 Uncertainty comparison of different undersampling ratios

The previous sections mainly evaluate the performance of the guided wavefield sparse reconstruction with two different undersampling ratios. Here, the uncertainty comparison of different undersampling ratios is made in terms of SNR using the same undersampling scheme. The purpose is to evaluate the capability of preserving the information content of signal while reducing the number of sampled points. Each experiment is randomly repeated 100 times, while the excitation frequency, the undersampling scheme and ratio remain unchanged but the distribution of the sampled points is random. Since the jittered scheme involves the sampling in a coarse grid and has a similar recovery accuracy, here we solely focus on the random scheme that can randomly samples in arbitrary undersampling ratio to map a relation between the undersampling ratio and SNR. Figs. 11 and 12 show the uncertainty comparison of different undersampling ratios in terms of SNR using the random scheme at 30 kHz and 50 kHz of central excitation frequency, respectively. The horizontal coordinate represents the underdetermined degree of the CS model, i.e., the undersampling ratio of the number m of the undersampling points to the number n of dense grid points (see Eq. (24)). The red curve is plotted by the averaged SNR of 100 repeated cases at each undersampling ratio. The discrete undersampling ratios are selected by changing the number of measurements as follows

$$Ratio = [100,200,272,300:100:1500]/2303 \times 100\% \quad (25)$$

There is a total of 16 discrete undersampling ratios on the interval [4.34%, 65.13%]. It is clear in Figs. 11 and 12 that the SNRs significantly increase as the increase of the sampled points. Meanwhile, the standard uncertainty of

SNRs has a trend of decrease as the increase of the sampled points. Particularly, the SNRs have a sharp increase on the interval [4.34%, 13.03%]. It means that the increase of the sampled points can improve the performance of the wavefield sparse reconstruction procedure. The recovery algorithm achieves high SNRs (nearly reaches 30 dB) when the number of sampled measurements m is sufficiently large. In such cases, one can observe that the recovery approach works well starting from more than 11.81 % measurements with respect to the original grid, where the averaged SNR at each undersampling ratio is over 15 dB. This is in line with the results reported in (Hennenfent and Herrmann 2008) for seismic data acquisitions.

We conduct the uncertainty comparison of different undersampling ratios ahead in the view of box plot. In the following, an interesting relationship between the undersampling ratio and the signal-to-reconstruction error-ratio will be modeled. First, we empirically find after abundant statistical experiments that there exists a linear function relation between the undersampling ratio and the reciprocal of the relation error, defined as

$$1/rel = a\times Ratio + b \tag{26}$$

where rel denotes the relation error between the reconstructed wavefield and the measured wavefield; parameters a and b denote the constant scalar coefficients of the first-order polynomial. Combing the expression of SNR in Eq. (23), one can get a simple formula

$$SNR = 20\cdot log(\,a\times Ratio + b) \tag{27}$$

The analytic formula in Eq. (26) is given by curve fitting methods instead of Eq. (27) on the specific interval $Ratio \in (11.81\%, 43.42\%)$, and further the SNRs of other undersampling ratios$Ratio \in (43.42\%, 65.13\%)$ can be estimated. The linear relation is obtained by using polynomials with proper orders to fit the mean of 100 values of $1/rel$ over the specific interval. Furthermore, the mapping relation in Eq. (27) can be obtained as shown in Figs. 13 and 14. The pointwise standard-error bands of light gray shades show the standard uncertainty interval $[mean - std, mean + std]$, the scatters denotes 100 SNRs at each undersampling ratio, and the light red shades presents the predicted SNRs by Eq. (27) on the interval $Ratio \in (43.42\%, 65.13\%)$. As can be observed in Figs. 13 and 14 that the true curves (in black) and the fitted curves (in red) have a good fit where the goodness of fit, namely the R-square R^2>0.98 on $(11.81\%, 43.42\%)$. Note that when R-square R^2 is close one, the fitting result is better. The detailed definition of R-square R^2 can be found in the textbook of statistics (Montgomery *et al*.

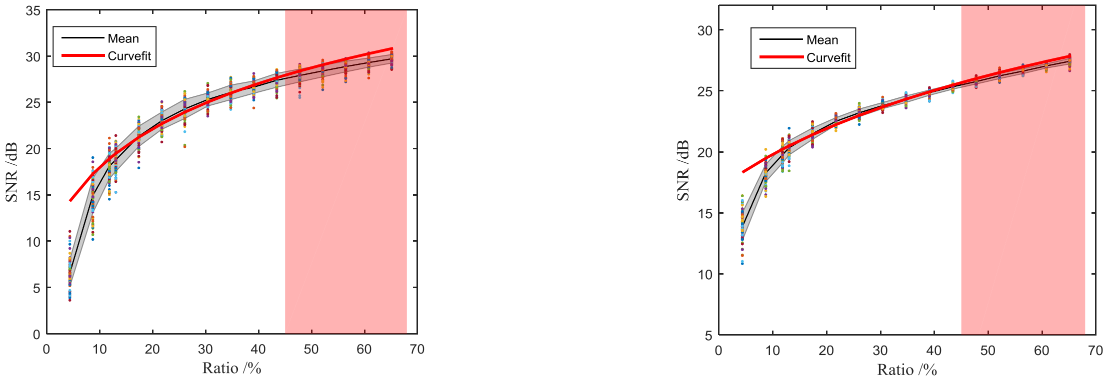

(a) *t* = 180.66 μs (b) *t* = 400.39 μs

Fig. 13 Map the relationship between SNR and the undersampling ratio at 30 kHz

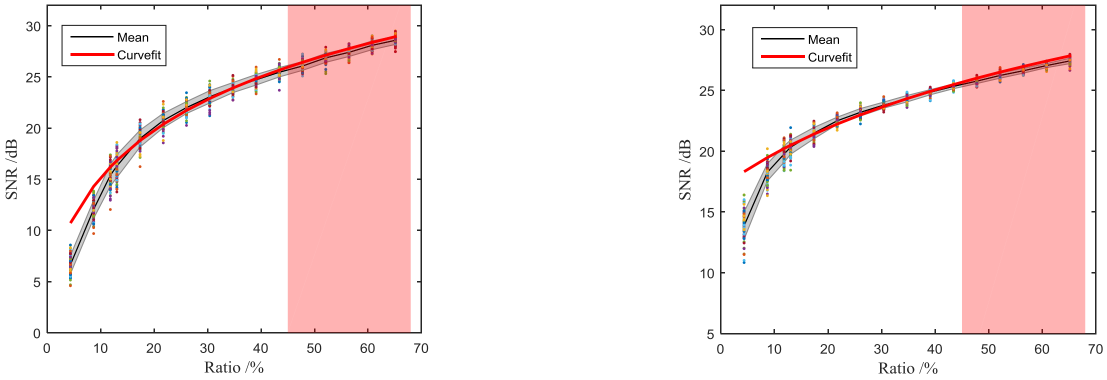

(a) *t* = 190.43 μs (b) *t* = 317.38 μs

Fig. 14 Map the relationship between SNR and the undersampling ratio at 50 kHz

2010). The predicted SNRs on $(43.42\%, 65.13\%)$ are nearly on the standard uncertainty interval of SNRs $[mean - std, mean + std]$. Therefore, one can conclude that the undersampling ratio on a specific interval is proportional to the reciprocal of the relation error of the reconstructed wavefield in high probability.

5. Conclusions

In this paper, a guided wavefield sparse reconstruction procedure is presented using compressed sensing for minimizing the number of sampling points. An underdetermined system of linear equations is solved in which there are fewer equations than unknowns in the compressed sensing frame. Three undersampling schemes, sparsity-promoting dictionary and the gradient projection approach are investigated to produce the best recovery of an undersampling wavefield obtained by the scanning laser Doppler vibrometer. The effectiveness and reliability of the sparse reconstruction approach are verified under different excitation frequencies, different wavefield snapshots, different undersampling schemes and different under-sampling ratios.

The experiments of guided wavefield reconstruction on an aluminum plate demonstrate that the proposed sparse reconstruction procedure succeeds in recovering the full wavefield from highly incomplete measurements with high accuracy, leading to dramatically reduced measurement points. In this case, 11.81% measurements can lead to a perfect full wavefield image that has a good match with the measured one by SLDV. Comparing with the regular undersampling scheme that fails to reconstruct the wavefield, both the random and jittered schemes following a discrete random uniform distribution have a higher SNR. The uncertainty comparison of different undersampling schemes shows that the jittered scheme that controls the gap of adjacent sampled points generally, has a higher SNR and a smaller uncertainty than the random scheme in terms of probability. For the same undersampling ratio, SNRs of the reconstructed results with different distributions of sampling points have a small deviation. The uncertainty comparison of different undersampling ratios shows that the increase of the undersampling points can generate a higher SNR and lead to a smaller uncertainty. There exists a simple analytic function relation between the undersampling ratio and the signal-to-reconstruction error-ratio on a specific interval in high probability. In this work, we focus on the sparse reconstruction of the guided wavefield on a pristine plate. In an ongoing work, we will evaluate the performance of the sparse reconstruction approach using compressed sensing on a damaged plate without baseline data.

Acknowledgments

The first author would like to acknowledge the support from the National Natural Science Foundation of China (No. 51705397) and China Postdoctoral Science Foundation (No. 2019T120900 & 2017M610636). The primary part of the presented work was completed during the first author's visit to the Structural Dynamics and Acoustic Systems Laboratory at the University of Massachusetts Lowell.

References

Alguri, K.S. and Harley, J.B. (2016), “Consolidating guided wave simulations and experimental data: a dictionary learning approach”, *Proceedings of SPIE Smart Structures and Materials, Nondestructive Evaluation and Health Monitoring*, 98050Y-98050Y-10. https://doi.org/10.1117/12.2219420

Beck, A. and Teboulle, M. (2009), “A fast iterative shrinkage-thresholding algorithm for linear inverse problems”, *SIAM J. Imaging Sci*., **2**(1), 183-202. https://doi.org/10.1137/080716542

Bioucas-Dias, J.M. and Figueiredo, M.A.T. (2007), “A new TwIST: Two-step iterative shrinkage/thresholding algorithms for image restoration”, *IEEE Transact. Image Process*., **16**(12), 2992-3004. https://doi.org/10.1109/TIP.2007.909319

Candes, E. and Romberg, J. (2007), “Sparsity and incoherence in compressive sampling”, *Inverse Probl*., **23**(3), 969.

Candes, E.J. and Wakin, M.B. (2008), “An introduction to compressive sampling”, *IEEE Signal Process. Mag*., **25**(2), 21-30. https://doi.org/10.1109/MSP.2007.914731

Chen, D.M., Xu, Y.F. and Zhu, W.D. (2018a), “Identification of damage in plates using full-field measurement with a continuously scanning laser Doppler vibrometer system”, *J. Sound Vib*., **422**, 542-567. https://doi.org/10.1016/j.jsv.2018.01.005

Chen, Y., Joffre, Y.D. and Avitabile, P. (2018b), “Underwater dynamic response at limited points expanded to full-field strain response”, *J. Vib. Acoust*., **140**(5), 051016. https://doi.org/10.1115/1.4039800

Di Ianni, T., De Marchi, L., Perelli, A. and Marzani, A. (2015), “Compressive sensing of full wave field data for structural health monitoring applications”, *IEEE Transact. Ultrason. Ferr. Freq. Control*, **62**(7), 1373-1383. https://doi.org/10.1109/TUFFC.2014.006925

Donoho, D. (2006), “Compressed sensing”, *IEEE Transact. Inform. Theory*, **52**(4), 1289-1306. https://doi.org/10.1109/TIT.2006.871582

Duarte, M.F., Davenport, M.A., Takhar, D., Laska, J.N. and Sun, T. (2008), “Single-pixel imaging via compressive sampling”, *IEEE Signal Process. Mag*., **25**(2), 83-91. https://doi.org/10.1109/MSP.2007.914730

Figueiredo, M.A.T., Nowak, R.D. and Wright, S.J. (2007), “Gradient projection for sparse reconstruction: Application to compressed sensing and other inverse problems”, *IEEE J. Select. Topics Signal Process.*, **1**(4), 586-597. https://doi.org/10.1109/JSTSP.2007.910281

Flynn, E.B. and Jarmer, G.J. (2013), “High-speed, non-contact, baseline-free imaging of hiddden defects using scanning laser measurements of steady state ultrasonic vibration”, *Struct. Health Monit*., **1**, 1186-1193.

Ginsberg, D., Fritzen, C.P. and Loffeld, O. (2018), “Sparsity-constrained extended Kalman filter concept for damage localization and identification in mechanical structures”, *Smart Struct. Syst., Int. J.*, **21**(6), 741-749. https://doi.org/10.12989/sss.2018.21.6.741

Harley, J.B. (2016), “Predictive guided wave models through sparse modal representations”, *Proceedings of the IEEE*, **104**(8), 1604-1619. https://doi.org/10.1109/JPROC.2015.2481438

Hennenfent, G. and Herrmann, F.J. (2008), “Simply denoise: wavefield reconstruction via jittered undersampling”, *Geophysics*, **73**(3), 19-28. https://doi.org/10.1190/1.2841038

Herrmann, F., Friedlander, M. and Yilmaz, O. (2012), “Fighting the curse of dimensionality: Compressive sensing in exploration seismology”, *IEEE Signal Process. Mag*., **29**(3), 88-100.

10.1109/MSP.2012.2185859

Hong, M., Mao, Z., Todd, M.D. and Su, Z. (2017), "Uncertainty quantification for acoustic nonlinearity parameter in Lamb wave-based prediction of barely visible impact damage in composites", *Mech. Syst. Signal Process.*, **82**, 448-460. https://doi.org/10.1016/j.ymssp.2016.05.035

Kim, S.J., Koh, K., Lustig, M., Boyd, S. and Gorinevsky, D. (2007), "An interior-point method for large-scale l1-regularized least squares", *IEEE J. Select. Topics Signal Process.*, **1**(4), 606-617.

Kirkup, L. and Frenkel, R.B. (2006), *An Introduction to Uncertainty in Measurement: using the GUM (guide to the expression of uncertainty in measurement)*, Cambridge University Press.

Lu, Y., Ye, L., Wang, D., Zhou, L. and Cheng, L. (2010), "Piezo-activated guided wave propagation and interaction with damage in tubular structures", *Smart Struct. Syst., Int. J.*, **6**(7), 835-849. https://doi.org/10.12989/sss.2010.6.7.835

Mesnil, O. and Ruzzene, M. (2016), "Sparse wavefield reconstruction and source detection using compressed sensing", *Ultrasonics*, **67**, 94-104. https://doi.org/10.1016/j.ultras.2015.12.014

Montgomery, D.C., Runger, G.C. and Hubele, N.F. (2010), *Engineering Statistics*, (5th Edition), John Wiley & Sons.

Park, H.J., Sohn H., Yun, C.B., Chung, J. and Kwon, I. (2010), "A wireless guided wave excitation technique based on laser and optoelectronics", *Smart Struct. Syst., Int. J.*, **6**(5-6), 749-765. https://doi.org/10.12989/sss.2010.6.5_6.749

Park, B., An, Y.K. and Sohn, H. (2014), "Visualization of hidden delamination and debonding in composites through noncontact laser ultrasonic scanning", *Compos. Sci. Technol.*, **100**, 10-18. https://doi.org/10.1016/j.compscitech.2014.05.029

Perelli, A., Di Ianni, T., Marzani, A., De Marchi, L. and Masetti, G. (2013), "Model-based compressive sensing for damage localization in Lamb wave inspection", *IEEE Transact. Ultrason. Ferr. Freq. Control*, **60**(10), 2089-2097. 10.1109/TUFFC.2013.2799

Qiao, B., Chen, X., Luo, X. and Xue, X. (2015), "A novel method for force identification based on the discrete cosine transform", *J. Vib. Acoust.*, **137**(5), 051012. https://doi.org/10.1115/1.4030616

Qiao, B., Zhang, X., Gao, J., Liu, R. and Chen, X. (2016a), "Impact-force sparse reconstruction from highly incomplete and inaccurate measurements", *J. Sound Vib.*, **376**, 72-94. https://doi.org/10.1016/j.jsv.2016.04.040

Qiao, B., Zhang, X., Wang, C., Zhang, H. and Chen, X. (2016b), "Sparse regularization for force identification using dictionaries", *J. Sound Vib.*, **368**, 71-86. https://doi.org/10.1016/j.jsv.2016.01.030

Qiao, B., Zhu, M., Liu, J., Zhao, Z. and Chen, X. (2019), "Group sparse regularization for impact force identification in time domain", *J. Sound Vib.*, **445**, 44-63. https://doi.org/10.1016/j.jsv.2019.01.004

Sohn, H., Dutta, D., Yang, J.Y., DeSimio, M., Olson, S. and Swenson, E. (2011), "Delamination detection in composites through guided wave field image processing", *Compos. Sci. Technol.*, **71**(9), 1250-1256. https://doi.org/10.1016/j.compscitech.2011.04.011

Song, W., Xiang, J. and Zhong, Y. (2017), "Mechanical parameters detection in stepped shafts using the FEM based IET", *Smart Struct. Syst., Int. J.*, **20**(4), 473-481. https://doi.org/10.12989/sss.2017.20.4.473

Staszewski, W., Lee, B., Mallet, L. and Scarpa, F. (2004), "Structural health monitoring using scanning vibrometry: I. Lamb wave sensing", *Smart Mater. Struct.*, **13**(2), 251-260.

Su, Z., Ye, L. and Lu, Y. (2006), "Guided Lamb waves for identification of damage in composite structures: A review", *J. Sound Vib.*, **295**(3-5), 753-780. https://doi.org/10.1016/j.jsv.2006.01.020

Tropp, J. and Wright, S.J. (2010), "Computational methods for sparse solution of linear inverse problems", *P. IEEE*, **98**(6), 948-958. 10.1109/JPROC.2010.2044010

Wright, S.J., Nowak, R.D. and Figueiredo, M.A.T. (2009), "Sparse reconstruction by separable approximation", *IEEE Transact. Signal Process.*, **57**(7), 2479-2493. https://doi.org/10.1109/TSP.2009.2016892

Xiang, J., Matsumoto, T., Long, J. Wang, Y. and Jiang, Z. (2012), "A simple method to detect cracks in beam-like structures", *Smart Struct. Syst., Int. J.*, **9**(4), 335-353. https://doi.org/10.12989/sss.2012.9.4.335

Xiang, J., Nackenhorst, U., Wang, Y., Jiang, Y., Gao, H. and He, Y. (2014), "A new method to detect cracks in plate-like structures with though-thickness cracks", *Smart Struct. Syst., Int. J.*, **14**(3), 397-418. https://doi.org/10.12989/sss.2014.14.3.397

Xu, C., Yang, Z., Chen, X., Tian, S. and Xie, Y. (2018), "A guided wave dispersion compensation method based on compressed sensing", *Mech. Syst. Signal Process.*, **103**, 89-104. https://doi.org/10.1016/j.ymssp.2017.09.043

Yang, Z.B., Radzienski, M., Kudela, P. and Ostachowicz, W. (2017), "Damage detection in beam-like composite structures via Chebyshev pseudo spectral modal curvature", *Compos. Struct.*, **168**, 1-12. https://doi.org/10.1016/j.compstruct.2017.01.087

Yang, Z., Yu J., Tian, S., Chen, X. and Xu, G. (2018), "A damage localization method based on the singular value decomposition (SVD) for plates", *Smart Struct. Syst., Int. J.*, **22**(5), 621-630. https://doi.org/10.12989/sss.2018.22.5.621

Yang, Z.B., Wang, Z.K., Tian, S.H. and Chen, X.F. (2019), "Analysis and modelling of non-Fourier heat behavior using the wavelet finite element method", *Materials*, **12**(8), 1337. https://doi.org/10.3390/ma12081337

BS